Wear Behavior of AlSi10Mg Alloy Produced by Laser-based Powder Bed Fusion and Gravity Casting

Pietro Tonolini, Dr. Lorenzo Montesano, Dr. Marialaura Tocci, Prof. Annalisa Pola, Prof. Marcello Gelfi*

Department of Mechanical and Industrial Engineering, University of Brescia, via Branze 38, 25123 Brescia, Italy

E-mail: p.tonolini002@unibs.it

Keywords: LPBF, AlSi10Mg, wear, heat treatments, T6

Abstract

In this work, the sliding wear behavior of AlSi10Mg samples realized using laser-based powder bed fusion (LPBF) is investigated via pin on disc (PoD) tests, before and after T6 heat treatment. The changes in the microstructure, density, and hardness induced by heat treatment are correlated with the tribological behavior of the alloy. Furthermore, short wear tests are performed and the resulting wear tracks are investigated through scanning electron microscopy (SEM), equipped with an energy dispersive spectroscopy (EDS) microprobe to elucidate how the wear mechanisms evolved with sliding distance. For comparison, gravity cast (GC) AlSi10Mg samples are also characterized and tested.

The as-built AM sample exhibits the lowest wear rate and coefficient of friction because of its high hardness and relative density while the heat-treated sample shows the worst behavior in comparison with the GC samples. The results suggest a significant influence of porosity on the wear behavior of AM alloys.

1. Introduction

Laser-based powder bed fusion of metal (PBF-LB/M or simply LPBF) — also known as direct metal laser sintering (DMLS) or selective laser melting (SLM) — is an additive manufacturing

This article has been accepted for publication and undergone full peer review but has not been through the copyediting, typesetting, pagination and proofreading process, which may lead to differences between this version and the Version of Record. Please cite this article as doi: 10.1002/adem.202100147.

(AM) method. The LPBF process uses a powder bed and laser source to achieve layer-by-layer selective fusion and subsequent building of near-net-shape 3D objects from input CAD data [1]. Compared to conventional manufacturing processes, such as casting or forging, this technique allows much greater freedom of design and a lower need for subsequent machining operations, thus reducing material wastage, as well as good mechanical properties [2-4].

Currently, different metallic powders can be processed using this manufacturing method. Stainless steel [5], Ti [6], Co [7], Ni [8], and Al [9] alloys have been widely investigated in the literature, and Cu [10], Mg [11], and Au [12] alloys are attracting increased interest. The LPBF technique can be applied in the fields of aerospace [13], aviation [14], and automotive [15] industries, as well as the production of robotic components [16], orthopedic implants [17], or simple prototypes [18].

Regarding the automotive field, according to the new target to reduce CO_2 passenger car emissions from 2025 to 2030, established by EU regulations [19], there is a need to further reduce car weight to minimize harmful emissions and improve fuel economy. As a rule of thumb, fuel savings of 4 % can be achieved by reducing the vehicle's mass by 10 % [20]. Therefore, the use of aluminum and low-density alloys is continuously growing to replace ferrous components in the automotive industry [21]. In this context, AM technology allows the enhancement of mechanical properties and the development of even lighter structures through topological optimization or lattice structures [22, 23], with respect to conventional casting methods. Based on this, the further use of this technology can help achieve a more significant weight reduction of Al components.

AlSi10Mg is a typical heat-treatable gravity cast (GC) alloy that is widely used owing to its good castability, low thermal expansion, good mechanical properties, and significant corrosion resistance [24]. This alloy usually undergoes T6 heat treatment, consisting of solution treatment, quenching, and artificial aging, to achieve better mechanical performance. AlSi10Mg alloy is also the most widely used and investigated Al alloy for the AM process [25].

Several works are available in the literature on comparing the properties of LPBF and GC AlSi10Mg samples, both in the as-produced and heat-treated state. In these studies, it was reported

that the extremely fine microstructure that characterizes the as-produced LPBF parts promotes better mechanical properties, such as higher tensile strength and hardness [26], impact resistance [27], and cavitation erosion resistance [28]. However, the fatigue strength is comparable between different production processes [29]. The effect of conventional T6 heat treatment on the mechanical properties has also been widely studied and is correlated with the microstructural evolution during heat treatment [26, 28-32]. It is well documented that the solution treatment of GC samples enhances their strength and hardness due to the precipitation of the Mg_2Si phase, in conjunction with the spheroidization of Si particles [33]. In contrast, the microstructure coarsening and disruption of the Si network — which occurs during the solution treatment of the AM samples — softens the material, which becomes more ductile and less resistant with respect to the as-produced condition [26, 30-32]. Moreover, it has been demonstrated that AM AlSi10Mg exhibits a certain degree of porosity [34] that can grow during T6 treatment owing to the high-temperature exposure, thus contributing to the above-mentioned reduction in mechanical properties compared to the as-built condition [30]. In contrast, a similar behavior during heat treatment has not been detected in GC AlSi10Mg because of the different manufacturing methodologies, notwithstanding the existence of porosity in GC parts [30].

Despite the high number of studies on AlSi10Mg alloy, only some works are available in the literature regarding the comparison of sample wear resistance achieved by AM or GC. Many studies have been conducted on AlSi10Mg matrix composites reinforced with micro-or nano-ceramic particles realized through LPBF technology but not on the bulk alloy. In these studies, the addition of different amounts of TiC [35, 36], TiB_2 [37-39], AlN [40], and SiC [41-43] particles have been extensively studied owing to the resulting material wear resistance enhancement due to the reduced coefficient of friction from the presence of small well-dispersed ceramic particles with respect to the bulk material.

However, the use of composite materials is not always straightforward and is inconvenient if several components require high wear resistance. For instance, automotive-coupled parts, such as

pistons and cylinders (which can experience wear during service), are currently produced by the casting process of conventional Al alloys. In such cases, topologically optimizing these parts, together with the enhanced mechanical properties achieved through AM processes, could reduce the weight of the components and increase their performance if the material exhibits adequate wear resistance.

In this regard, the recent research by Sagbas et al. [44] evaluated the effect of different surface finishing operations on the wear resistance of AlSi10Mg samples produced through LPBF technology. However, this study does not consider the heat treatment effect or the comparison of wear behavior with the same conventional casting alloy.

To date, the only work in the literature comparing the wear resistance of Al-alloy AM and GC samples, both in the as-produced state and after T6 thermal treatment, involves the AlSi12 alloy [45]. The absence of Mg in the alloy leads to a different strengthening mechanism, both in the as-produced AM and heat-treated condition with respect to AlSi10Mg, where Mg_2Si precipitation can occur [46]. This lack of systematic experimental tests and deep analysis of the wear behavior of the LPBF-AlSi10Mg alloy represents a limitation to the identification of further and alternative applications of this alloy. Therefore, this work aimed to investigate the effect of microstructure, hardness, and porosity level on the wear resistance of additive manufacturing AlSi10Mg samples, in both as-produced and T6 heat-treated conditions. Samples obtained via conventional gravity casting in the as-cast condition and after T6 heat treatment were also considered for comparison.

2. Materials and methods

AlSi10Mg alloy samples were produced through additive manufacturing (AM) and traditional gravity casting (GC) routes.

Laser-based powder bed fusion (LPBF) technology has been used for AM sample production. Commercially available gas atomized AlSi10Mg powder was processed using an EOS M290 machine (400 W, Yb laser fiber; F-theta lens; 30 A and 400 V power supply; 7000 hPa, 20 m^3 h^{-1}

inert gas supply; 100 μm focus diameter; EOS GmbH Electro Optical System [47]). Gravity cast samples were machined from an industrial component produced in a steel permanent mold and cut from areas of the casting with the same thickness (20 mm) to avoid different solidification conditions and, thus, different microstructures between samples. The AM samples had a square cross-section of 12 mm × 12 mm and a length of 57 mm, with their long sides parallel to the building platform. The same geometry was chosen for the GC samples. The chemical compositions of the samples were assessed by optical emission spectroscopy and are reported in **Table 1**.

Table 1. Mean chemical composition [wt. %] of samples produced by additive manufacturing (AM) and gravity casting (GC).

	Si	Mg	Fe	Mn	Cu	Zn	Pb	Al
AM	10.245	0.396	0.212	0.002	0.001	<0.002	<0.002	Balance
GC	9.375	0.313	0.422	0.227	0.066	0.053	0.009	Balance

T6 was performed on a set of both AM and GC samples by using optimized heat treatment parameters derived from previous work on AlSi10Mg alloy [30]. In particular, the heat treatment comprised a solution treatment at 540 °C for 1 h, followed by quenching in water at 65 °C and a final aging at 180 °C for 2 h.

Microstructural characterization was performed on samples in both as-produced and T6 conditions while density and hardness values were derived from a previous work that studied the optimization of heat treatment parameters for the same treated alloy manufactured in the same job [30]. In particular, density measurements were conducted by weighing the samples in air and distilled water and applying Archimedes' law, as usually performed to estimate the quality of AM parts [48-50]. The relative density was calculated by dividing the measured mean density by the theoretical alloy density (2.68 g/cm^3). The sample hardness was obtained as the average of five Brinell indentations (62.5 kg and 2.5 mm carbide ball), according to the ASTM E10 standard.

The specimens were polished to a mirror finish for microstructural characterization, which was conducted using an optical microscope Leica DMI 5000M (Leica Microsystem) equipped with image analyzer LAS software and a scanning electron microscope (LEO EVO 40, Zeiss). For the

AM T6 sample, a deeper analysis of the evident and large porosity observed in the microstructure was performed using the image analyzer LAS software to evaluate the distribution and mean equivalent diameter of the pores. AM samples in the as-produced condition were etched with Keller reagent for 30 s to reveal the melting pools, Si network, and Si particles [51].

To evaluate the wear behavior, pin-on-disk (PoD) dry wear tests were performed using a THT tribometer (CSM Instruments) equipped with a stylus profilometer (TRIBOtechnic) to record the wear track profile at the end of each test. Regarding AM samples, both the horizontal and vertical sections of the material were tested to investigate the influence of the building direction on the wear properties. Both the AM and GC specimens were tested in the as-produced and heat-treated states. Each sample was first ground with SiC papers of up to 800 grit to obtain Ra<0.8 µm. The PoD tests were conducted according to the ASTM G99 standard [48], using a 100 Cr6 steel ball with a 6 mm diameter as the counterpart. The coefficient of friction (CoF) was calculated during the tests by recording the frictional force. Each test was performed using a constant load of 5 N, applied for a sliding distance of 500 m at a linear velocity of 0.2 m s^{-1}. The radius of the wear track was 3.5 mm. Tests were repeated at least twice for each material condition and five track profile measurements were conducted in different positions for each test to calculate the mean value and standard deviation of the cross-sectional area of the track. By multiplying this value for the circumference of the track, the material loss volume was determined and the wear rate was calculated, as reported in [53]. To investigate the wear mechanisms, short wear tests (sliding distances of 10, 80, and 250 m) were conducted to observe the wear tracks at the beginning of the wear damage using a scanning electron microscope (SEM, LEO EVO 40, Zeiss) integrated with an energy dispersive spectroscopy microprobe (EDS, Oxford Instruments). Finally, cross sections of the tested samples were analyzed at the end of the test by SEM to further investigate the wear mechanism. In addition, cross section of AM-xy and AM-z samples were observed under optical microscope after 10 m of sliding distance in order to detect the role of microstructural feature on wear behavior at the beginning of the test.

3. Results and discussion

3.1 Microstructure

The vertical cross-section of the AM sample etched by Keller's reagent (**Figure 1a**) shows typical semi-circular melt pools, with melt pool boundaries in a lighter gray, while the fine microstructure cannot be resolved at this magnification owing to the rapid and repeated heating/cooling cycles. On the horizontal cross-section (**Figure 1b**), elongated scan tracks can be recognized according to the pattern followed by the laser when building the samples. The boundary between neighboring melt pools (or scan tracks), their size, and microstructure depends on the power of the laser and the building strategy of the components [37, 54]. Furthermore, in agreement with the literature, some small pores, typical of the production process, can be observed within the melt pools (Figure 1). The presence of spherical pores is due to the agglomeration and coalescence of entrapped bubble gas in the melt pools [55]. The gas can be either the process of inert gas or gas impurities present in the LPBF chamber, as residual air. Gas entrapment occurs as a result of melt splashing, capillary effect (Marangoni flow), and vaporization of low-melting-point constituents present in the powder or to its residual humidity (hydrogen adsorption) [55-57]. Furthermore, few non-spherical cavities were detected in the sample structure because of shrinkage and/or lack of fusion phenomena during the layer-by-layer building process [58-61].

At higher magnification (**Figure 3a**), it is possible to observe a fine network of interconnected Si particles, typical of AlSi10Mg AM alloys in the as-built condition [30].

Figure 1. AM as-produced samples: a) vertical and b) horizontal cross-section. White arrows put in evidence small pores.

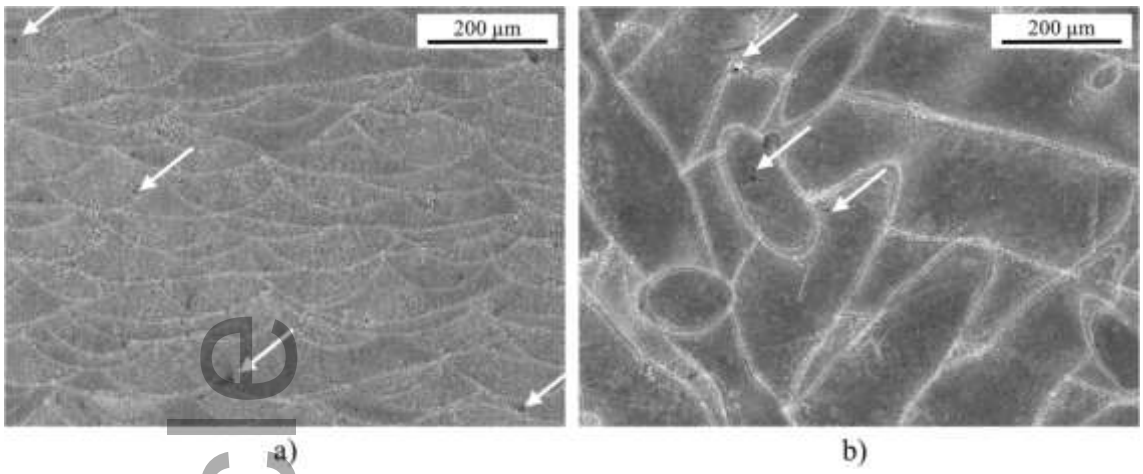

Considering the microstructure of the AM sample under the T6 condition (**Figure 2**), owing to the exposure at high temperatures, larger and more abundant pores can be observed with respect to the as-produced sample, as expected from the literature [30, 57]. Furthermore, T6 heat treatment led to the homogenization of the microstructure, making the melt pool boundaries no longer visible, and promoting significant coarsening and spheroidization of the Si particles (**Figure 3b**).

As confirmed by a recent XRD analysis conducted by the authors [62] on samples fabricated in the same job as those studied in this work, an increase in the Si volume fraction is detected after T6 heat treatment. The as-built non-equilibrium condition, promoted by the rapid solidification mechanism, is characterized by a high amount of Si retained in the solid solution together with Al lattice distortion. This condition is quickly recovered during T6 heat treatment, leading to the coarsening and spheroidization of the Si particles [62].

Figure 2. a) Microstructure and b) SEM image of AM samples after T6 treatment. White arrows indicate small pores.

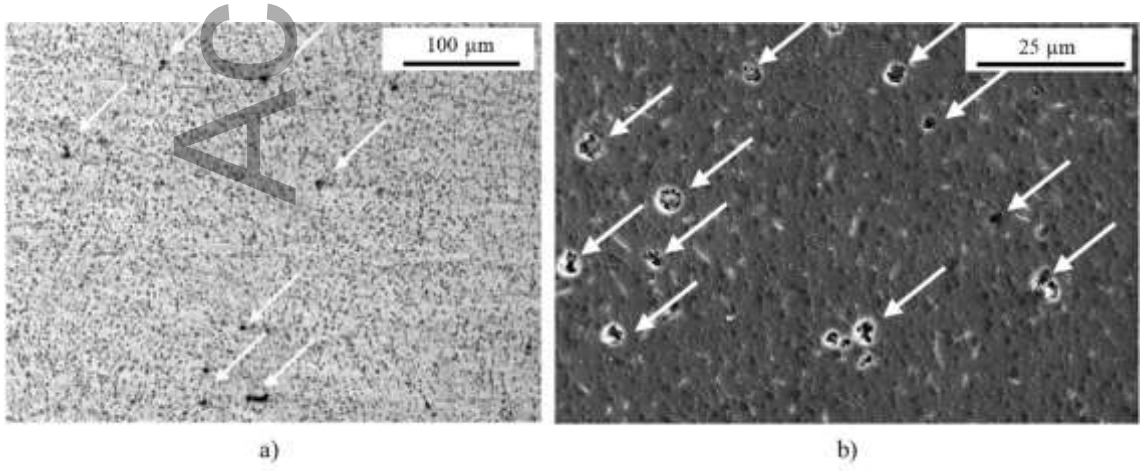

Figure 3. SEM image of a) AM as-produced and b) AM T6 sample.

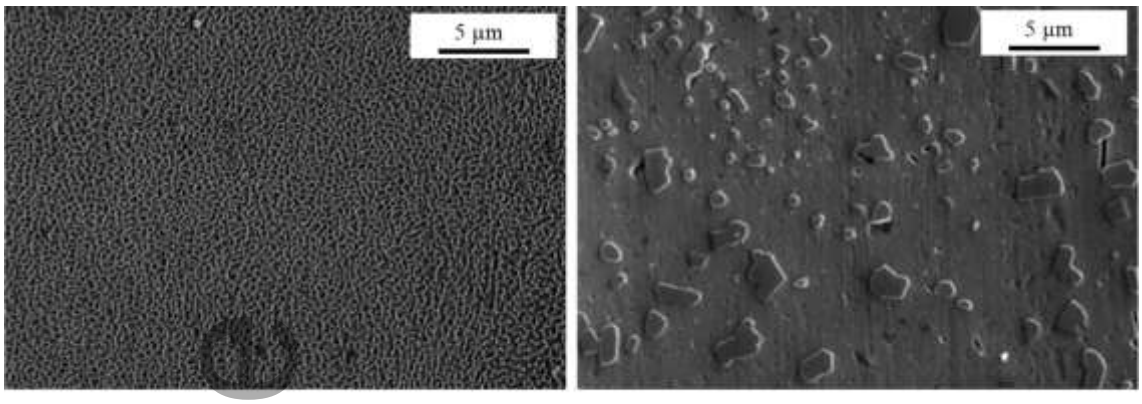

The microstructure of the GC samples in the as-cast condition (**Figure 4a**) exhibits typical Al dendrites surrounded by the eutectic mixture; Fe intermetallics are also visible (for example, those highlighted by the arrows in Figure 4). As for the AM samples, T6 heat treatment promoted the spheroidization of the Si particles; however, contrary to AM, no growth of pores was detected. (**Figure 4b**).

Figure 4. GC samples in a) as-cast condition and b) after T6 treatment. White arrows indicate Fe-rich intermetallics.

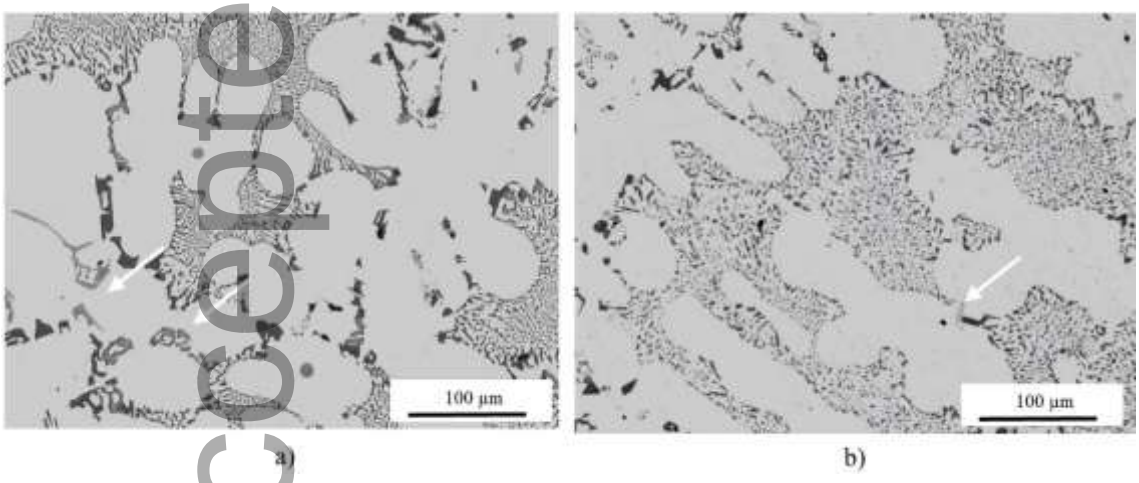

3.2 Density and hardness

The densities of the samples and corresponding relative densities are reported in **Table 2**.

Table 2 Density of considered samples [30].

		Density [g cm $^{-3}$]	Relative density %
AM	as-produced	2.679±0.003	99.9 ± 0.1
	T6	2.618±0.006	97.7 ± 0.2

GC	as-produced	2.669±0.006	99.6 ± 0.2
	T6	2.668±0.008	99.5 ± 0.3

Density measurements confirmed the highest porosity level of the AM-T6 sample, as suggested by microstructural characterization (Figure 2). The density of the AM-T6 sample was 2.2 % lower than that in the as-produced condition. In particular, image analysis of the AM-T6 sample showed that pores are distributed in the matrix with a density of 256 pores mm^{-2}, characterized by a mean equivalent diameter of 7.00 ± 2.45 μm and an approximately spherical shape (i.e., a width/height ratio of 1.4 ± 0.3); this is typical of gas pores, as can be observed from Figure 2. This increase in material porosity is not surprising and has already been reported in the literature for Al [30, 57] and Ti [63] alloys produced via additive manufacturing. Two main mechanisms have been proposed to explain this phenomenon. The rapid solidification experienced by AM samples promotes an increase in the retained hydrogen in the alloy, which can exceed the equilibrium solubility of the solid phase [57]. Therefore, in the as-built AM samples, a certain quantity of H can be found in the supersaturated Al solid solution. During T6 treatment, the holding of the alloy at 540 °C for 1 h promoted the transition from this metastable state to an equilibrium condition. This causes pore formation and a consequential reduction in the relative density after T6 [30, 57]. Furthermore, the inert gas (Ar), which is insoluble in the molten alloy, can be trapped in the molten pools and form gas pores. When the alloy is heat-treated, the pressure inside the existing gas pores increases owing to the expansion of the entrapped gas at high temperatures. If this pressure increases above the yield strength of the material at the treatment temperature, an increase in the volume of the pores occurs, resulting in a further decrease in the density of the material. These phenomena likely occurred during the solution treatment of AM samples performed in the present study and determined the documented decrease in density after T6 treatment.

Conversely, this does not happen for GC samples because the solidification rate is much lower than that during the AM process, promoting equilibrium conditions in the as-cast material. The density

difference for the GC samples before and after T6 treatment was negligible. Finally, it is interesting to observe that the AM and GC specimens in the as-produced condition exhibited a comparable density (with a variation of less than 0.4 %).

Figure 5 shows the results of the hardness measurements. No evident correlation between density and hardness was found, which is in agreement with other studies [16]. The AM sample after T6 heat treatment showed the lowest density but the highest hardness of approximately twice that of the as-produced GC sample, despite their comparable density.

The remarkable hardness of the as-produced AM sample is related to several strengthening mechanisms, induced by the rapid solidification of the alloy, such as solid-solution and dislocation strengthening mechanisms, residual stresses, and those related to the ultra-fine grain size of the material [46, 65]. It is well known that a very fine grain size implies a high density of grain boundaries, which act as barriers to dislocation motion, promoting a higher material hardness [65, 66]. Furthermore, the rapid cooling and subsequent reheating of the alloy during the LPBF process is responsible for the formation of Mg_2Si precipitates, in the same way as it takes place during the solution and aging treatment. Hence, intrinsic heat treatment often occurs during the building process [67].

As confirmed by recent TEM analysis, the precipitated Mg_2Si colonies are effective in increasing the strength of the material by hindering the movement of dislocations [46].

After T6 heat treatment, the AM hardness decreased by 11.9 % compared to the as-produced condition (Figure 5). This result is consistent with the literature [26, 30-32], which reported similar material softening after T6 heat treatment of AM samples. This behavior can be attributed to the evolution of the microstructure after solution treatment (Figure 1b) and thus to the different contributions of the strengthening mechanisms acting in the as-produced AM samples when compared to the heat-treated sample, as further supported by the XRD analysis published by the authors [62].

The coarsening of the microstructure and disruption of the Si network after the solution treatment involves a reduction in grain boundary density and a loss of melt pool boundaries (Figure 2), reducing their effectiveness as a barrier to dislocation movement. Therefore, the decrease in hardness measured for the T6 AM sample confirms that the strengthening effect due to precipitation aging cannot compensate for the softening effect due to coarsening of the original AM microstructure, as discussed in the literature [65].

As expected, the hardness of the as-cast GC sample (63.4 ± 1.5 HB) was enhanced by 69.7 % after solution treatment. Finally, the same hardness value was achieved after the heat treatment for AM and GC samples, 110.1 ± 1.1 HB and 107.6 ± 6.5 HB, respectively, despite the differences in size and shapes of the Si particles, which appear to have a minor influence on material hardness [26, 30].

Figure 5. Brinell hardness values of studied samples [30].

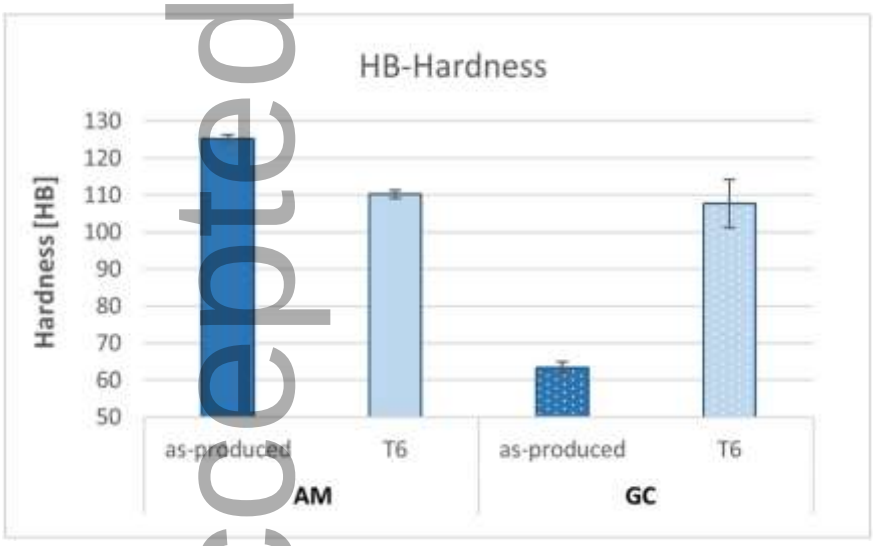

3.3 Wear resistance

Figure 6 shows the evolution of the friction coefficient (CoF) with the sliding distance for all tested samples. All curves exhibit the typical shape of sliding wear for Al alloys [68].

A high CoF was recorded at the beginning of the test owing to the presence of asperities between the two contact surfaces. Subsequently, it progressively decreased because of the fragmentation of these asperities under compression and shear stress. This occurs approximately in the first 80 m of

testing while the CoF reaches a steady-state condition afterward. All tested samples exhibited the same behavior.

Figure 6. Coefficient of friction tendency with sliding distance. Arrows indicate the distance chosen for shorter tests and SEM analysis.

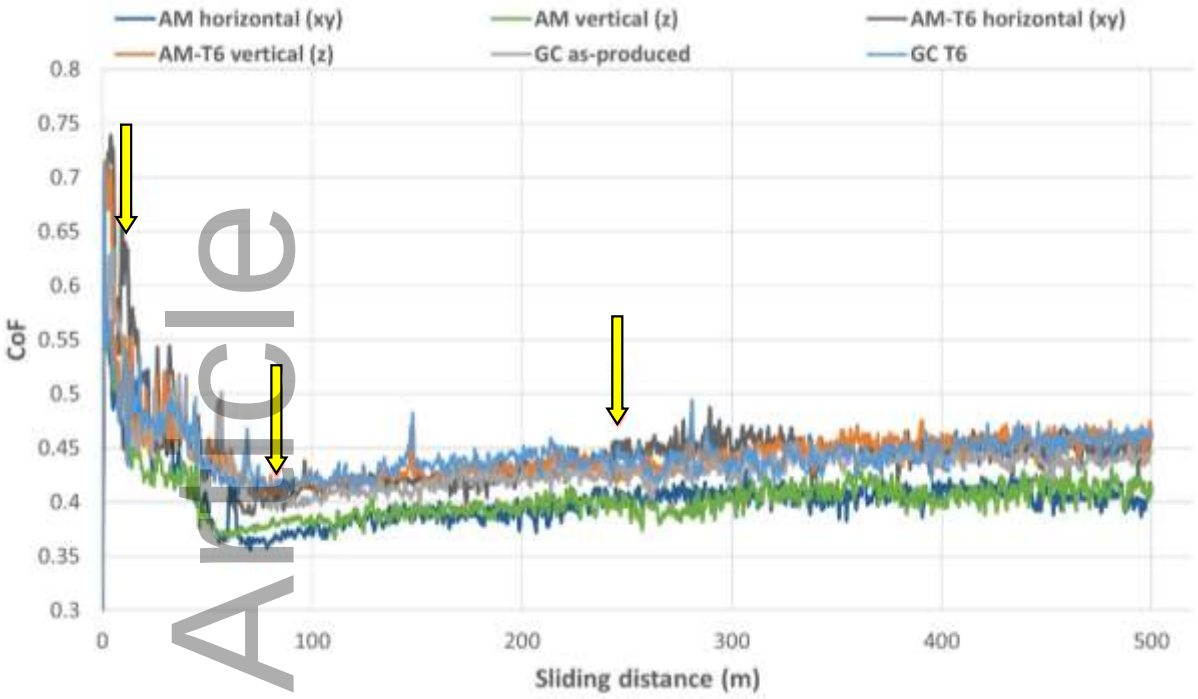

The mean values of the steady-state CoF for the tested samples are presented in **Table 3**. The as-produced AM samples exhibited the lowest CoF (0.40). No significant difference in terms of CoF was detected between the horizontal and vertical sections. The other tested samples were characterized by slightly higher CoF values (approximately 0.44). Interestingly, the same value of CoF was measured for AM-T6 and GC samples, despite the different microstructures and hardness. This behavior is correlated with the formation of aluminum oxide layers on the sliding surfaces of both pin and discs materials, as documented in the SEM analysis presented in the next paragraphs. In fact, the steady state CoF values measured for the various samples are similar to that obtained at room temperature for Al_2O_3 sliding against Al_2O_3 i.e. 0.4 [80]

Table 3. Coefficient of friction for the investigated samples.

			CoF	St. Dev.
AM	as-produced	horizontal (xy)	0.399	0.014
		vertical (z)	0.402	0.011
	T6	horizontal (xy)	0.440	0.015
		vertical (z)	0.442	0.014
GC	as-produced		0.446	0.020

T6		0.440	0.011

The mean wear rate at 500 m is shown in **Figure 7**, together with the hardness (HB) and the relative density for each tested sample (due to a scale effect, the relative density standard deviation presented in Table 2 is not visible in the plot). At the end of the wear tests, there was no substantial difference in wear behavior between the horizontal and vertical AM specimens, both in the as-produced and after T6 heat treatment conditions, contrary to what is typically detected for tensile [54] and impact [67] properties.

The as-produced AM samples are characterized by the lowest wear rate (~2.15×10^{-4} mm^3 N^{-1} m^{-1}), promoted by the high hardness and density. After T6 heat treatment, the AM samples exhibit the highest wear rate (~7.33×10-4 mm^3 N^{-1} m^{-1}) compared to both the as-produced AM samples and GC alloy.

This behavior can be correlated with the microstructural evolution and porosity growth (97.7% relative density) of the AM alloy during heat treatment. The lower dislocation density of the T6 samples was promoted by the loss of the extra-fine microstructure [62, 71] and the other strengthening contribution related to the fast solidification resulted in a lower hardness, explaining the poor wear resistance of this sample [75]. Furthermore, the presence of a significant number of porosities reduces alloy wear resistance because they enhance material removal during testing, as reported by other authors [45, 76]. The presence of porosities on the tested surface reduces the load-bearing area, leading to higher local stresses applied to the material and, consequently, to a higher wear rate [70].

The crucial role of porosity on material performance is also supported by the different responses of the GC samples after heat treatment as compared to the AM-T6 samples. Although GC-T6 samples exhibit almost the same hardness as AM-T6 samples, the former are characterized by a lower wear rate. From a microstructural point of view, the materials under the T6 condition present the same strengthening mechanism in both cases, based on the formation of Mg_2Si precipitates during aging.

However, the AM-T6 sample is characterized by a more uniform distribution of Si particles, which should represent a load-bearing phase; therefore, they were expected to be positive in terms of wear resistance. Conversely, the porosity of the AM-T6 samples was approximately 2.5 %, which was significantly higher than that of the GC-T6 samples (approximately 0.5 %). Based on these data, the higher wear rate of AM-T6 suggests that the porosity is particularly deleterious to material behavior. Finally, as expected, the GC-T6 samples exhibited a lower wear rate than the GC alloy in the as-produced condition because the heat treatment-induced Al matrix strengthening and spheroidization of the Si particles.

Therefore, comparing the AM and GC heat-treated samples, which are characterized by the same steady-state CoF values and similar hardness, it is possible to confirm the assumption that the porosity level plays a key role in determining the material wear behavior. In particular, a density difference of approximately 2 % corresponds to a difference in the wear rate of approximately 51 %, indicating the importance of a very dense material for wear resistance applications.

Figure 7. Wear rate (mm^3 N^{-1} m^{-1}) after 500 m distance of the tested samples VS Hardness and relative density values.

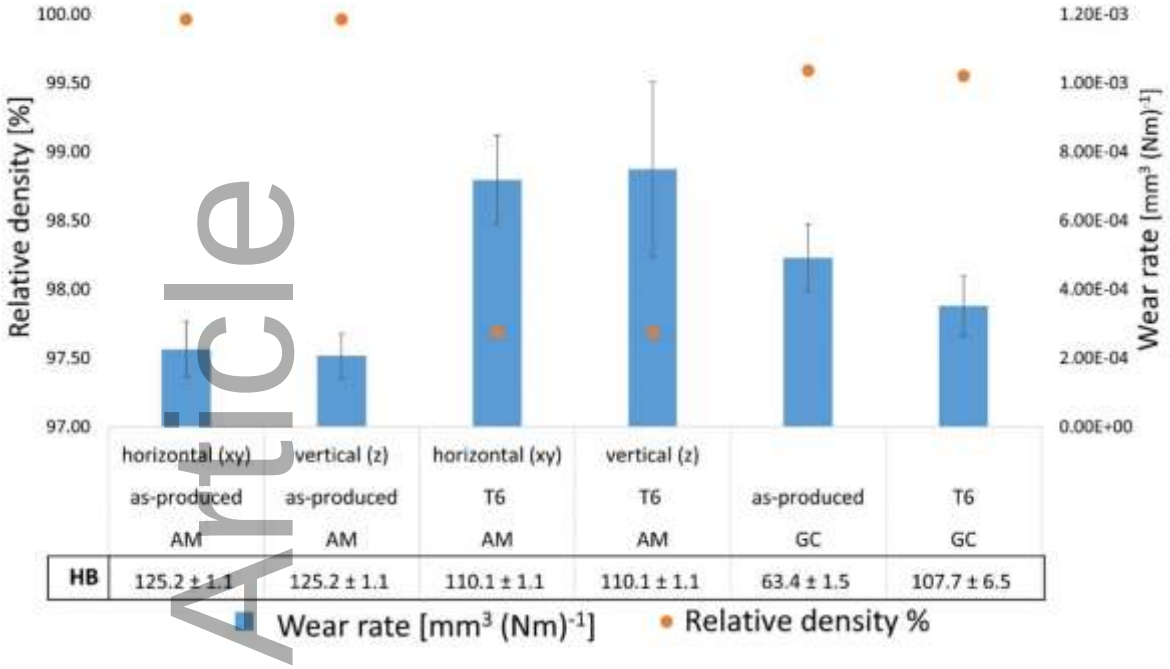

To better understand the evolution of the wear mechanism, PoD tests were repeated and interrupted at fixed distances of 10 m, 80 m, and 250 m (as indicated by the arrows in Figure 6) and the worn surface was analyzed by SEM for each sample. These three distances were selected according to the evolution of the CoF during the test (Figure 5), particularly when the CoF reached a specific level, i.e., close to the maximum (10 m), minimum (80 m), or steady-state (250 m). For the three sliding distances, the SEM images and EDS analyses (% wt) are reported in **Figures 8, 11**, and **12**, respectively.

Figure 8 shows the presence of coarse wear particles ejected from the wear track surface after a sliding distance of 10 m, likely due to the removal of asperities; this is consistent with the high value of the CoF measured at the beginning of the test (Figure 6). Adhesion layers were visible in the worn tracks for all the investigated samples, indicating that adhesion wear is the primary mechanism. In addition, the low oxygen content measured by EDS analysis suggests that the worn surface was not significantly oxidized.

Figure 8. SEM images of wear tracks after 10 m testing for samples a) AM-xy, b) AM T6-xy, c) AM-z, d) AM T6-z, e) GC, and f) GC T6

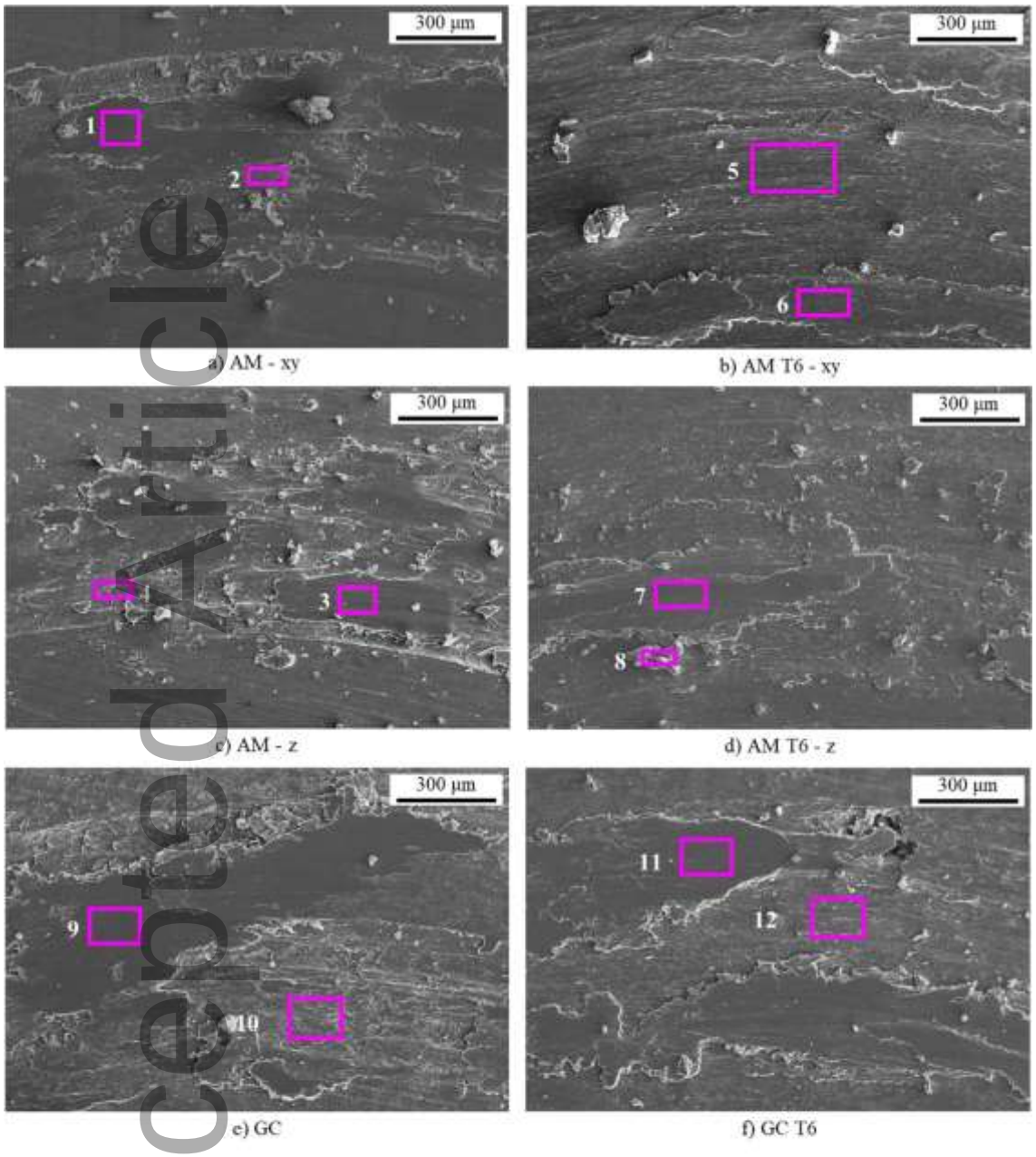

Spectrum	1	2	3	4	5	6	7	8	9	10	11	12
O	8.48		8.99				4.72		7.4			12.2
Al	81.8	89.44	80.76	89.31	85.99	86.58	84.19	89.35	82.53	83.37	85.8	78.35
Si	9.72	10.56	10.26	10.69	14.01	13.42	11.09	10.65	10.07	16.63	14.2	9.44

Regarding the as-produced AM samples, the cross-sections of tested samples were also observed to investigate the influence of the surface orientation and melt pool boundary. Interestingly, it can be noted that the melt pool boundaries influence material removal during the wear tests (**Figures 9 and 10**), acting as a barrier to plastic deformation, especially for sliding on the horizontal section

(Figure 9); this could be due to the finer grain size along the melt pool boundaries when compared to the center of the melt pool. Melt pool boundaries are characterized by extremely fine equiaxed grains [72]. This indicates a high density of grain boundaries, which has been reported to enhance wear resistance, as discussed by Liu et al. [73] in a study on selective laser melted AlSi10Mg. This is also in agreement with the findings of Rathod et al. [45] on AlSi12 alloys, who further discussed that boundary orientation influences crack propagation. However, no information about crack propagation can be inferred from the analysis presented in this study.

Figure 9. Cross-sections of as-produced AM-xy sample after 10 m sliding distance.

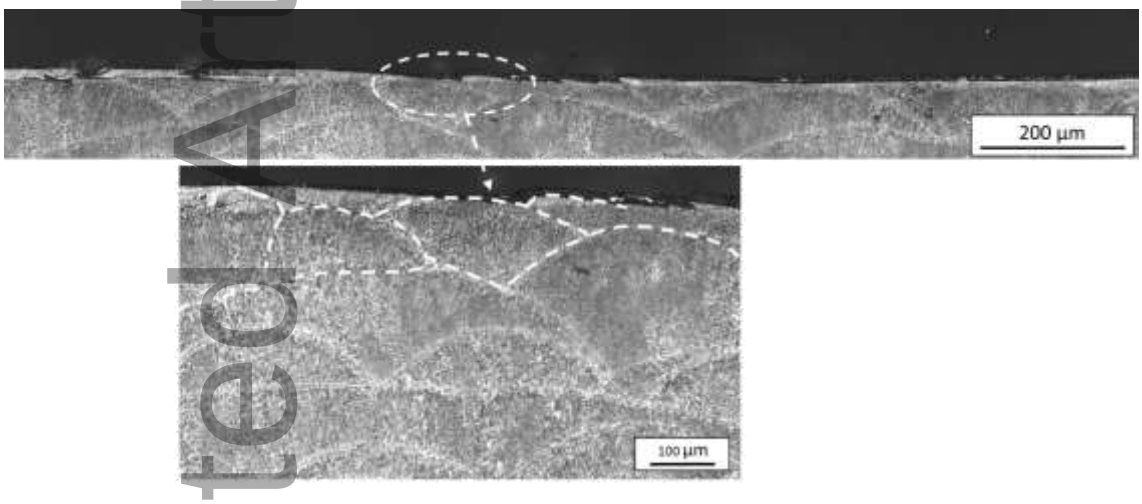

Figure 10. Cross-sections of as-produced AM-z sample after 10 m sliding distance.

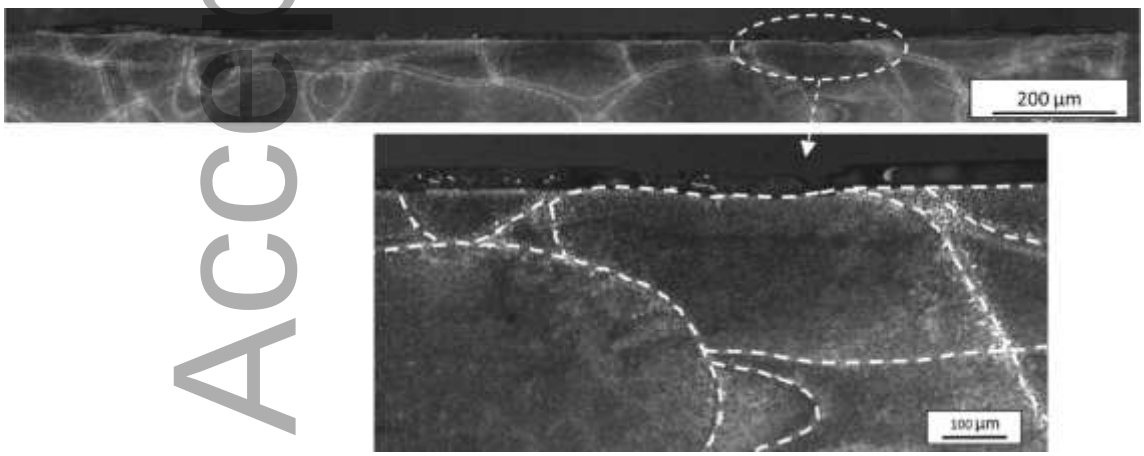

As the sliding distance increased to 80 m, areas with a relevant oxygen content became evident on the worn surface (**Figure 11**), suggesting the formation of an oxide layer. The high coefficient of friction, registered up to a sliding distance of 80 m, generates significant frictional heat that promotes the reaction between Al and O present in the environment, forming aluminum oxide.

Furthermore, some authors [64] also reported that the wear debris released by the adhesive mechanism in the first stage of the slow velocity sliding test oxidizes owing to their high reactivity. This debris can re-stick on the worn surface during the subsequent passages of the pin, promoting the more-or-less continuous formation of an oxide layer and adhering to the tested material.

The brittle oxide was progressively broken and removed during the wear test, producing fine debris particles. Given the absence of oxide layers on the wear tracks after 10 m of testing (Figure 8), it can be assumed that the oxidation of the worn surface took place between 10 m and 80 m, with a consequent decrease in CoF, as measured up to 80 m (Figure 6), due to the contact between the oxidized wear debris adherent to the worn surface of 100Cr6 ball and the oxide layers formed on the wear tracks.

Finally, EDS analysis of the gravity casting samples revealed a small amount of Fe and Mn that is related to the presence of intermetallic particles, as already noticed by the optical microscope analyses (Figure 4). Such Fe-Mn-rich precipitates, due to their relative high hardness, can improve the wear resistance of the GC T6 alloy [24] with respect to the AM T6 sample that is almost free from intermetallics because of its lower Fe and Mn content as a consequence of the different feedstock material production route.

Figure 11. SEM images of wear tracks after 80 m testing for samples a) AM-xy, b) AM T6-xy, c) AM-z, d) AM T6-z, e) GC and f) GC T6.

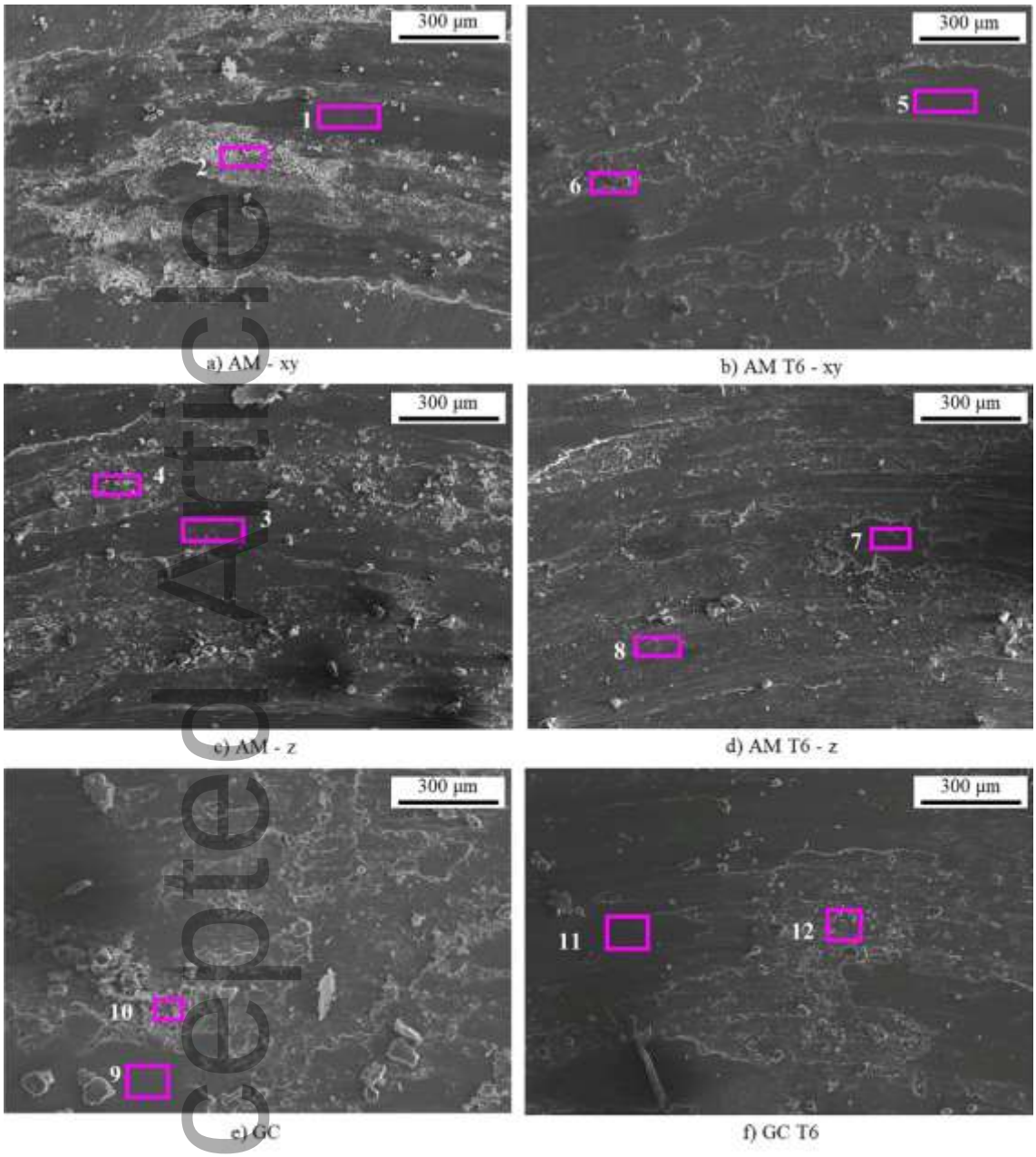

Spectrum	1	2	3	4	5	6	7	8	9	10	11	12
O	20.58	26.01	10.81	8.81	23.92	8.53	20.38	1.4	9.54	26.82	15.77	
Mg								0.39				
Al	71.23	67.43	80.54	83.14	67.98	80.45	70.44	83.58	74.81	65.99	74.39	87.43
Si	8.18	6.56	8.65	8.05	8.1	11.02	9.18	14.63	14.95	7.18	9.85	11.3
Mn									0.69			0.67
Fe												0.61

SEM images and EDS analyses of the worn tracks after 250 m showed relevant oxidation of the surface (**Figure 12**); this indicates that the pin interacts with the oxide layer on the surface instead of the alloy beneath. Furthermore, also the worn scar on the steel ball at the end of the test for each

tested samples (**Figure 13**) showed oxidized Al adhesion layers indicating that no direct metal-on-metal contact occurs at this stage. No substantial difference was found in the worn surface morphology between different tested conditions. The CoF trend presented in Figure 6, suggests that the formation of the oxide-oxide contact should have started after 80 m of sliding distance. Moreover, the formation of debris due to the cracking and delamination of some portions of oxidized material on the worn track can be responsible for the small increase in the CoF values recorded for longer tests.

No significant evidence of the abrasive wear mechanism is visible under these test conditions on the worn surface of both disc and pin materials. Tribo-oxidative wear appears to be the most relevant mechanism after 250 m. This is interesting because a previous work by the authors [74] on Al-Mg-Sc alloy produced by AM technology showed a different evolution of the wear mechanism, from adhesive to abrasive wear, and finally changed into a tribo-oxidative mechanism during the PoD test under analogous conditions. This difference can be explained by considering the microstructures of the two alloys. AlSi10Mg alloy is characterized by the presence of Si particles, which behave as a load-bearing phase, while the Al-Mg-Sc alloy consists of an Al-Mg solid solution strengthened by Sc-rich particles of nanometric size or, in any case, finer than the Si particles or network. In the latter case, debris particles are likely to be sufficiently harder than the Al-Mg solid solution to induce an abrasive mechanism whereas, for AlSi10Mg, this is hindered by the presence of Si particles, both as a network or disconnected particles [53].

Discussing the wear behavior of the AM samples before and after T6 heat treatment, the oxide layer formed on the as-built wear track seems to be more adherent and compacted with respect to the oxide layer formed on the heat-treated sample (Figure 12). This behavior can be related to the presence of a fine Si network in the as-built samples, which act as a more efficient load-bearing phase than the coarse and non-uniform distributed Si particles generated by T6 heat treatment. Moreover, the interface between the coarse Si particles and the Al matrix in the T6 samples can represent a preferential site for cracking during testing, leading consequently to oxide fragmentation

and delamination. This agrees with a recent study by Kan et al. [76], where cracking of Si particles in T6 specimens during sliding testing is documented.

Figure 12. SEM images of wear tracks after 250 m testing for samples a) AM-xy, b) AM T6-xy, c) AM-z, d) AM T6-z, e) GC and f) GC T6.

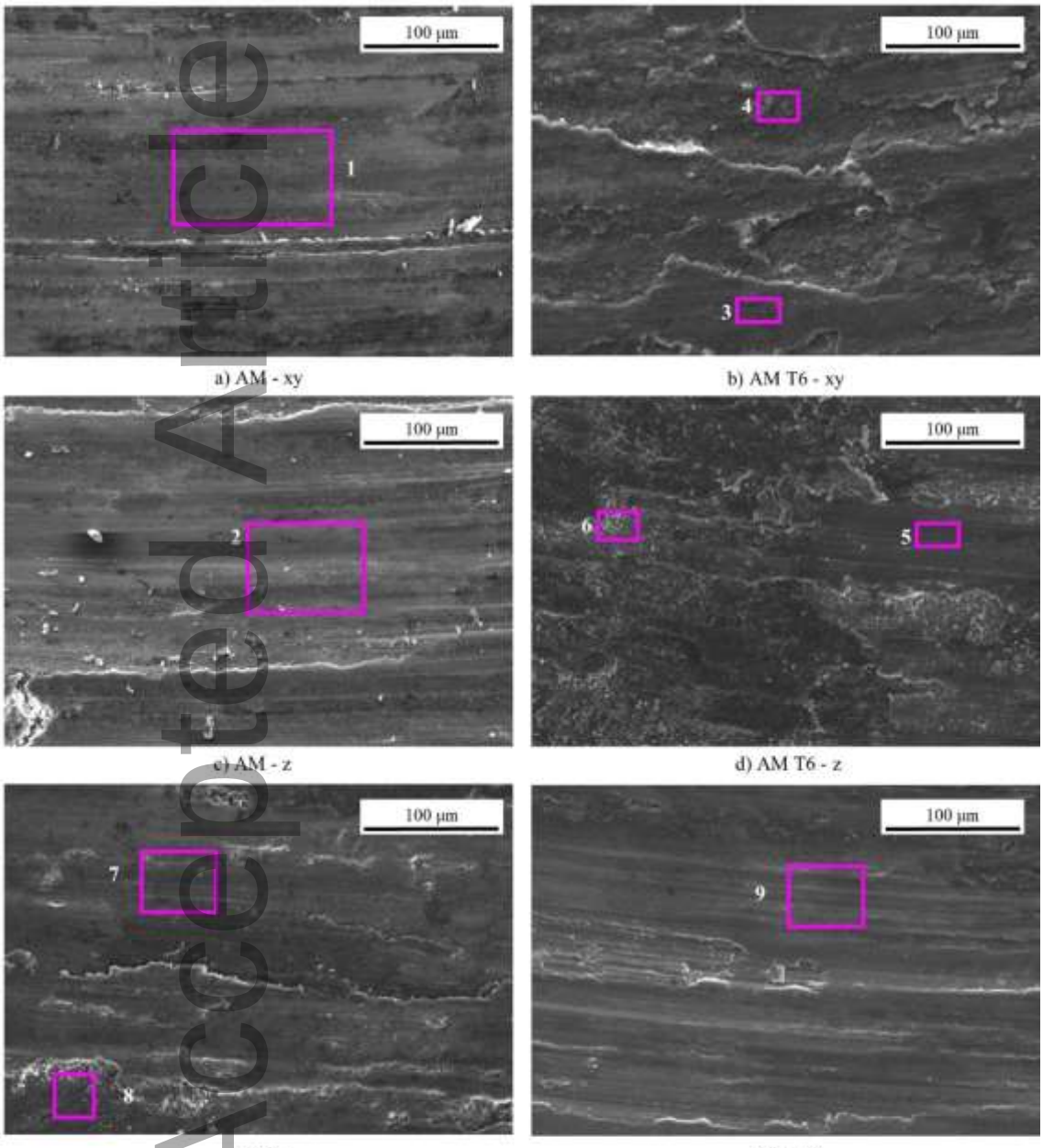

Spectrum	1	2	3	4	5	6	7	8	9
O	30.78	34.33	26.61	35.43	21.15	24.37	30.42	41.79	24.18
Al	61.77	59.35	61.34	59.23	65.05	67.18	61.12	52.26	66.3
Si	7.44	6.32	12.06	5.34	13.8	8.45	7.29	5.95	9
Mn							0.55		0.53
Fe							0.62		

Figure 13 SEM images of the 100Cr6 ball contact area at the end of the tests for samples a) AM -z, b) AM T6, c) GC and d) GC T6

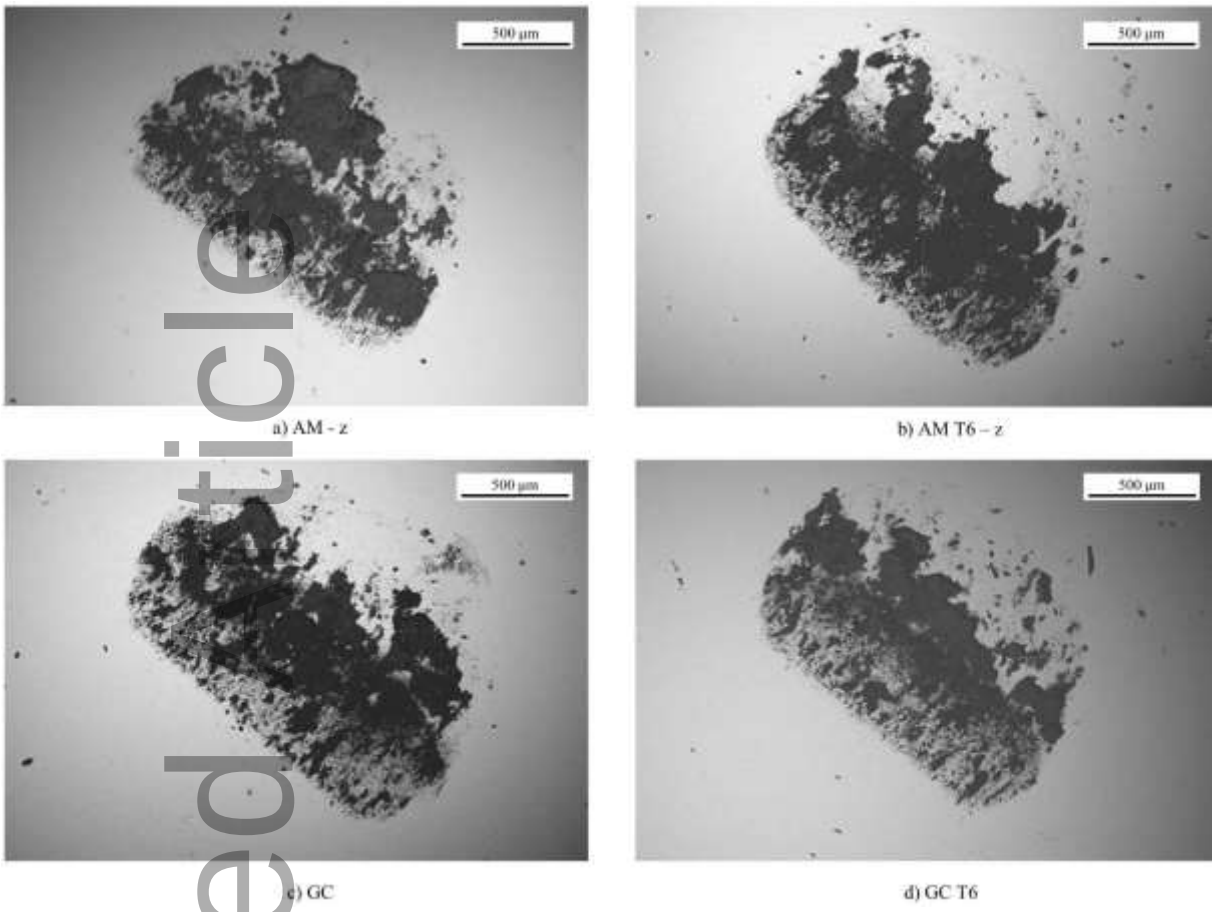

Furthermore, the detachment of a portion of the oxide layer on the worn surface of the heat-treated samples can be facilitated by the presence of some small pores on the surface, as indicated by the white arrows in **Figure 14**. This behavior can explain why the wear track after the same sliding distance is significantly larger (and deeper) for the AM-T6 samples than for the as-produced samples. This resulted in a higher wear rate at the end of the test. The influence of porosity on wear rate for AM Al-Si alloys was discussed by other authors [45, 76], who stated that emerging porosities are detrimental for wear resistance since they reduce the contact area and enhance sub-surface cracking.

Figure 14 SEM images. Detail of the worn surface after 250 m for the AM-T6 xy sample

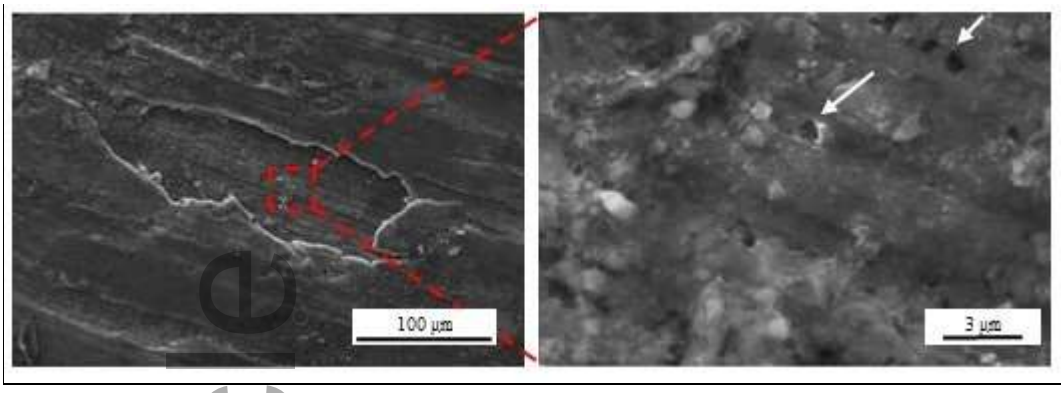

To verify this point, the analysis of the cross section of the samples at the end of the test was carried out and the related SEM images are shown in **Figure 15** for AM-z and GC sample under as-built and heat-treated conditions. It appears that the oxide layer for AM-z sample (Fig. 15 a) is particularly adherent to the substrate and continuous, as also suggested from the top view of the worn track. Analogous results were found for sample AM-xy, which are not reported for brevity sake.

On the contrary, for the AM T6-z sample the oxide layer appears more fragmented as shown by detachments from the substrate (Fig 15 b). The discontinuities represented by both porosities and Si particles enhance oxide fragmentation and delamination during testing, as revealed by Figure 16 a and Figure 16 b respectively, where white arrows indicate the crack propagation path.

The evidence of good adhesion of the oxide layer to the substrate is shown also in the case of GG and GC-T6 samples (Figure 15 c-d), but the oxide layer seems to be less compacted and uniform than for AM-z sample. It was also detected the presence of intermetallic particles at the interface between oxide layer and GC substrate that seems to act as initiation crack site for the oxide layer (Figure 16 c). On the other hand, intermetallic phases at the surface can act as load bearing phase thanks to their high hardness [81].

Figure 15 Cross-section SEM images of the wear track at the end of the test for samples a) AM-z, b) AM T6-z, c) GC and d) GC T6

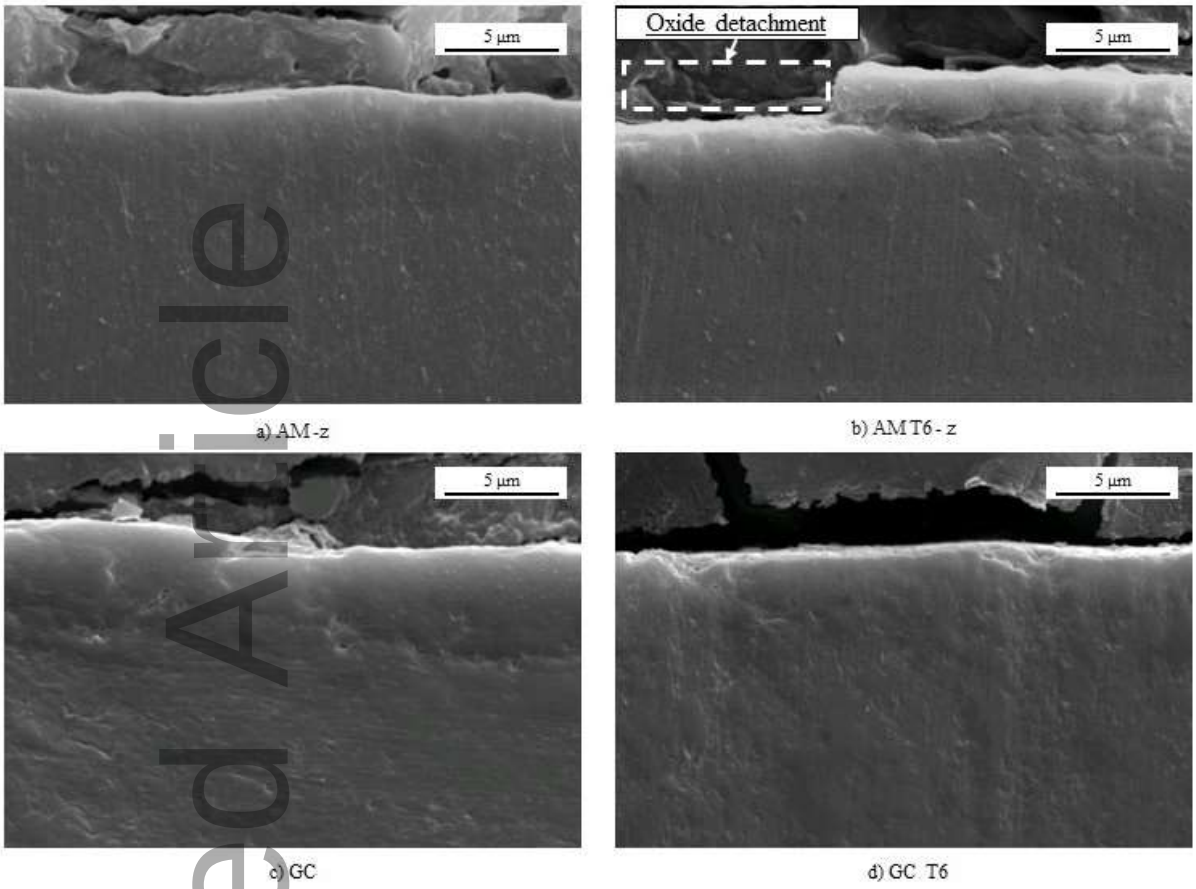

Figure 16 Particulars **of c**ross-section SEM images and EDS analysis of the wear track at the end of the test for samples a) AM-z, b) AM T6-z, c) GC T6

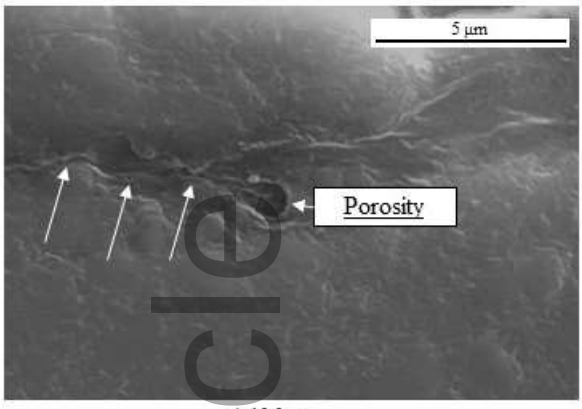

a) AM - z

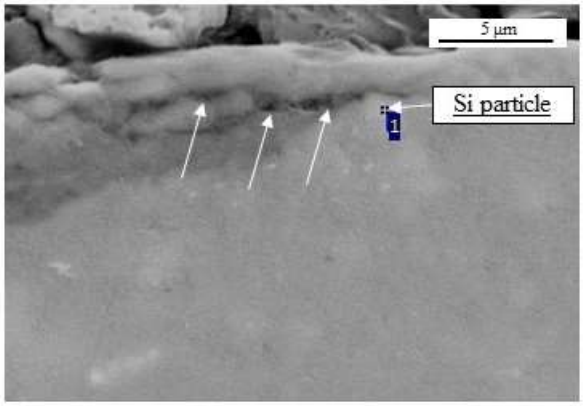

b) AM T6 - z

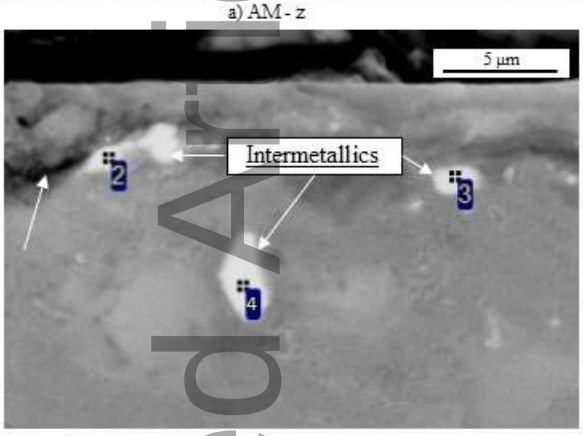

c) GC T6

Spectrum	1	2	3	4
O	16.85	20.30	14.45	-
Mg	0.25	0.11	0.10	0.22
Al	35.90	58.36	71.21	69.36
Si	46.99	8.17	9.54	10.48
Mn	-	4.43	1.97	6.94
Fe	-	8.63	2.73	12.99

In order to provide a complete overview of the wear behavior of the studied alloy in comparison with the literature, a list of published valuable works on the wear behavior of AM Al-Si alloys is summarized in **Table 4**.

Table 4. List of some published results regarding the wear behavior of LPDF Al-Si alloy.

Reference	Material	Production	Hardness	Relative density %	Counterpart	Wear rate [mm^{-3}/Nm]	Wear mode
Present work	AlSi10Mg	LPBF	125 HB	99.9	100Cr6 ball	2.2E-04	Adhesion/tribo-ox
Present work	AlSi10Mg	LPBF-T6	110 HB	97.7	100Cr6 ball	7.2E-04	Adhesion/tribo-ox
Present work	AlSi10Mg	GC	63 HB	99.6	100Cr6 ball	4.9E-04	Adhesion/tribo-ox
Present work	AlSi10Mg	GC-T6	107 HB	99.5	100Cr6 ball	3.5E-04	Adhesion/tribo-ox
[76]	AlSi10Mg	LPBF-Stress Relieved	135 HV	96.4 [77]	AISI 440C ball	9.2E-04	Adhesion/ tribo-ox
[76]	AlSi10Mg	LPBF-T6	110 HV	96.1 [77]	AISI 440C ball	7-9E-04	Adhesion/ tribo-ox
[78]	AlSi10Mg	LPBF	135 HV	Not measured	100Cr6 disk	1.17E-04	Abrasive/adesive/oxidation and delamination
[78]	AlSi10Mg	LPBF-T6	90 HV	Not measured	100Cr6 disk	1.23E-04	Abrasion/adhesion/oxidation and delamination
[79]	AlSi10Mg	LPBF	130 HV	Not measured	100Cr6 ball	4-5E-06	Adhesion/ tribo-ox
[73]	AlSi10Mg	LPBF	148 HV (sample A)	Not measured	SS disk	Not Available	Not Available
[36]	AlSi10Mg/TiC	LPBF	181.2 HV	98	100Cr6 ball	2.94E-05	Adhesion
[36]	AlSi10Mg/TiC	LPBF	167.5 HV	95	100Cr6 ball	5.50E-05	Adhesion
[75]	AlSi10Mg	LPBF	140 HV	99.6	Si_3N_4 ball	2.75E-04	Abrasion
[75]	AlSi10Mg	LPBF - T6	118 HV	Not measured	Si_3N_4 ball	4.90E-04	Abrasion
[45]	AlSi12	LPBF	125 HV	Not measured -	SS disk	8.12E-06	Abrasion
[45]	AlSi12	LPBF - T6	84 HV	Not measured	SS disk	9.10E-06	Abrasion
[53]	AlSi12	LPBF	105 HV	96	Al_2O_3 ball	7.0E-04	Abrasion
[53]	AlSi18	LPBF	80 HV	88	Al_2O_3 ball	9.00E-04	Abrasion

It is worth noting that Kan et al. [76], who studied the same tribological system used in the present work, found a higher wear rate for the as-built alloy as compared to the present work (Table 4).

This difference can be explained if the relative densities of the studied materials are considered. In fact, the samples tested in the present study are significantly denser that those considered in the work by Kan et al. (99.9 % vs 96.4%). As above mentioned, the presence of porosities plays a major role in the wear mechanisms since it determines a reduction in the loading area and this creates larger contact stresses, causing faster material removal. Furthermore, the presence of porosities represents an obstacle to the formation of a compact protective layer on the worn area and enhances oxide delamination and crack propagation. These mechanisms are likely responsible for the high wear rate recorded for the as-built sample in the study by Kan et al. On the other hand, when testing very dense materials, as for the as-built samples in the present study, the mechanisms above described do not take place. In this case, instead, a compact and protective oxide layer is observed on the wear track (Figure. 12 a,c and Figure 15 a), hindering material removal. Instead, when the porosity level is higher, as in the samples after T6 treatment, the performance is similar to that reported in the work of Kan et al. [76] (Table 4).

Tribological systems consisting in steel and AlSi10Mg alloy produced by L-PBF process are investigated in other studies listed in Table 4 [73, 78-79]. However, the AlSi10Mg alloy is used as pin instead of disk, as carried out in the present work. This leads to different contact mechanisms during sliding testing and different Hertzian stresses, which result in significantly lower measured wear rate. On the other hand, the wear mechanisms described in these works are similar to those detected in the present study, such as the formation of a protective oxide layer and adhesive wear mechanism [78-79].

In general, the differences in chemical composition of the tested alloys and wear test set-up, i.e., the material and dimensions of the counterpart, sliding method, number of cycles, etc., limit the possibility to directly compare the results of the other works listed in Table 4.

However, in other reported studies [45, 75], although the wear mechanisms are different from those identified in this work, it is worth noting that the T6 treatment on the AM AlSi10Mg sample

promotes a decrease in hardness and wear resistance as compared to the as-built sample , even if no decrease in relative density after T6 was measured. Hence, this further supports that the greater drop in wear resistance after heat treatment observed in the present work can be explained by the influence of increased porosity after T6, which determines a relative density reduction of 2 %. This is consistent with another study [36] on the wear behavior of AlSi10Mg/TiC composites realized by the AM method (Table 4). In this case, the density and hardness differences between the samples were derived from differences in the power of the laser used during the AM process. In particular, a reduction in hardness (8 %) and relative density (3 %) led to a wear resistance difference of approximately 47 %, which agrees with our results. Furthermore, the uniform distribution of strengthening TiC particles in the Al matrix resulted in low CoF and wear rate in comparison to the present study [36].

The microstructural evolution during T6 treatment (as discussed in the previous paragraph) and the consequent decrease in hardness and increase in porosity level appear to be responsible for the loss in wear resistance in comparison with the as-produced condition, as discussed above. Similar findings are also reported in studies on AlSi12 alloy produced by LPBF [45]. Considering the role of Si, the higher Si content likely contributes to the extremely low wear rate measured since Si behaves as a load bearing phase, especially when it is present as nanosized-particles as in the as-built condition [53]. However, it is not possible to make a direct comparison with the present work due to the different configuration of the tribological systems investigated (Table 4).

4. Conclusions

This work compares the sliding wear behavior of AlSi10Mg alloy realized by LPBF and gravity casting in both as-produced and T6 heat-treated conditions. The results of the PoD tests were discussed with respect to microstructure, density, and hardness of the different samples. The main conclusions are summarized as follows.

- All tested samples showed adhesive and tribo-oxidative wear mechanisms while abrasive wear was not detected.
- The AM as-built sample exhibited the best wear resistance while the heat-treated sample exhibited the worst wear resistance because of the hardness drop and significant increase in porosity.
- In the AM as-built sample, the melt pool boundaries are more wear-resistant than the center of the melt pool due to the presence of extremely fine equiaxed grains.
- The GC samples exhibited intermediate wear rates. Heat treatment increased the wear resistance of the material due to precipitation hardening in the alloy matrix.
- Since the AM and GC hardness values after T6 were comparable, the drop in wear resistance for the AM sample after T6 was mainly a consequence of the higher level of porosity.

Acknowledgments

The authors would like to thank Dr. L. Girelli and Ms. S. Al Balushi for their support in experimental activities and GHIAL S.p.A. for providing the casting samples.

Received: ((will be filled in by the editorial staff))
Revised: ((will be filled in by the editorial staff))
Published online: ((will be filled in by the editorial staff))

References

[1] *ISO / ASTM 52911 - 1:2019, Additive manufacturing - Design - Part 1: Laser-based powder bed fusion of metals*.

[2] J. P. Kruth, M. Badrossannay, E. Yasa, J. Deckers, L. Thijs, J. Van Humbeeck, *ISEM-XVI* **2010**, 3.

[3] O. Rehme, C. Emmelmann, Proc. SPIE. **2006**, 6107.

[4] E. O. Olakanmi, R. F. Cochrane, K. W. Dalgarno, *Prog. Mater. Sci.* **2015**, 74, 401.

[5] C. Zitelli, P. Folgarait, A. Di Schino, *Metals* **2019**, 9, 7.

[6] L. Zhang, H. Attar, Adv. Eng. Mater. **2016**, 18, 463.

[7] S. L. Sing, J. An, W. Y. Yeong, F. E. Wiria, *J. Orthop. Res*. **2016**, 34, 369.

[8] M. Elahinia, N. Shayesteh Moghaddam, M. Taheri Andani, A. Amerinatanzi, B. A. Bimber, R. F. Hamilton, *Prog. Mater. Sci*. **2016**, 83, 630.

[9] N. T. Aboulkhair, M. Simonelli, L. Parry, I. Ashcroft, C. Tuck, R. Hague, *Prog. Mater. Sci.* **2019**, 106, 100578.

[10] T. Q. Tran, A. Chinnappan, J. K. Y. Lee, N. H. Loc, L. T. Tran, G. Wang, V. V. Kumar, W. A. D. M. Jayathilaka, D. Ji, M. Doddamani, S. Ramakrishna, *Metals.* **2019**, 9, 7, 756.

[11] R. Karunakaran, S. Ortgies, A. Tamayol, F. Bobaru, M. P. Sealy, *Bioact. Mater.* **2020**, 5, 44.

[12] U. E. Klotz, D. Tiberto, and F. Held: *Gold Bull.* **2017**, 50, 111.

[13] T. E. Shelton, D. J. Stelzer, C. R. Hartsfield, G. R. Cobb, R. P. O'Hara, C. D. Tommila, *Rapid Prototyp. J.*, **2019**, 26, 557.

[14] P. Rokicki, B. Kozik, G. Budzik, T. Dziubek, J. Bernaczek, L. Przeszlowski, O. Markowska, B. Sobolewski, A. Rzucidlo, *Aircr. Eng.* **2016**, 88, 397.

[15] C. D. Naiju, M. Adithan, P. Radhakrishnan, and Y. U. Sravan, *Adv. Mater. Res.* **2012**, 383, 6242.

[16] D. Manfredi, F. Calignano, E. P. Ambrosio, M. Krishnan, R. Canali, S. Biamino, M. Pavese, E. Atzeni, L. Iuliano, P. Fino, C. Badini, *Metall. Ital.* **2013**, 10, 15.

[17] S. L. Sing, J. An, W. Y. Yeong, F. E. Wiria, *J. Orthop. Res.* **2016**, 34, 369.

[18] J. Sedlak, V. Sekerka, M. Slany, K. Kouril, O. Zemcik, J. Chladil, L. Rozkosny, *Acta Polytech.* **2015**, 55, 260.

[19] European Commission, CO_2 emission performance standards for car and vans (2020 onwards), https://ec.europa.eu/clima/policies/transport/vehicles/regulation_en#tab-0-0. Accessed March **2020**.

[20] A. Kastensson, *J. Cleaner Prod.* **2014**, 66, 337.

[21] Aluminium Insider, Aluminium Demand In Automotive Sector To More Than Double By 2025: Novelis' Labat, https://aluminiuminsider.com/aluminium-demand-in-automotive-sector-to-more-than-double-by-2025-novelis-labat/. Accessed March **2020**.

[22] T. Stankovic, J. Mueller, P. Egan, K. Shea, *J. Mech. Des*. **2015**, 137.

[23] A. du Plessis, I. Yadroitsava, I. Yadroitsev, *Opt. Laser Technol.* **2018**, 108, 521.

[24] ASM Specialty Handbook: Aluminum and Aluminum Alloys, ASM International **1993**, 579.

[25] F. Trevisan, F. Calignano, M. Lorusso, J. Pakkanen, A. Aversa, E.P. Ambrosio, M. Lombardi, P. Fino, D. Manfredi, *Materials* **2017**, 10(1), 76

[26] N. T. Aboulkhair, I. Maskery, C. Tuck, I. Ashcroft, N. M. Everitt, *Mater. Sci. Eng. A* **2016**, 667, 139.

[27] K. Kempen, L. Thijs, J. Van Humbeeck, J. P. Kruth, *Phys. Procedia* **2012**, 39, 439.

[28] L. Girelli, M. Tocci, L. Montesano, M. Gelfi, A. Pola, *Wear* **2018**, 402, 124-136.

[29] S. Beretta, S. Romano, *Int. J. Fatigue* **2017**, 94, 178.

[30] L. Girelli, M. Tocci, M. Gelfi, A. Pola, *Mater. Sci. Eng. A* **2019**, 739, 317.

[31] G. Ozer, G. Tarakci, M. S. Yilmaz, Z. C. Oter, O. Surmen, Y. Akca, M. Coskun, E. Koc, *Mater. Corros.* **2019**.

[32] X. Yu and L. Wang, *Procedia Manuf.* **2018**, 15, 1701.

[33] G. E. Totten, in *Heat Treating of Nonferrous Alloys* Vol. 4, ASM International, **2016.**

[34] N.T. Aboulkhair, N.M. Everitt, I. Ashcroft, C. Tuck, *Addit. Manuf.* **2014**, 1, 77.

[35] D. Gu, H. Wang, D. Dai, F. Chang, W. Meiners, Y.-C. Hagedorn, K. Wissenbach, I. Kelbassa, R. Poprawe, *J. Laser Appl.* **2015**, 27.

[36] D. Gu, H. Wang, F. Chang, D. Dai, P. Yuan, Y.-C. Hagedorn, W. Meiners, *8th International Conference on Laser Assisted Net Shape Engineering (Lane 2014)* **2014**, 56, 108.

[37] M. Lorusso, A. Aversa, D. Manfredi, F. Calignano, E. P. Ambrosio, D. Ugues, M. Pavese, *J. Mater. Eng. Perform.* **2016**, 25, 3152.

[38] M. Lorusso, A. Aversa, G. Marchese, F. Calignano, D. Manfredi, M. Pavese, *Adv. Eng. Mater.* **2020**, 22.

[39] L. Xi, S. Guo, D. Gu, M. Guo, K. Lin, *J. Alloys Compd.* **2020**, 819.

[40] D. Dai, D. Gu, M. Xia, C. Ma, H. Chen, T. Zhao, C. Hong, A. Gasser, R. Poprawe, *Surf. Coat. Technol.* **2018**, 349, 279.

[41] O. H. Famodimu, M. Stanford, C. F. Oduoza, L. Zhang, *Front. Mech. Eng.* **2018**, 13, 520.

[42] D. Gu, Y. Yang, L. Xi, J. Yang, M. Xia, *Opt. Laser Technol.* **2019**, 119.

[43] G. Xue, L. Ke, H. Zhu, H. Liao, J. Zhu, X. Zeng, *Mater. Sci. Eng. A* **2019**, 764.

[44] B. Sagbas, *Met. Mater. Int.* **2020**, 26, 143.

[45] H. J. Rathod, T. Nagaraju, K. G. Prashanth, U. Ramamurty, *Tribol. Int.* **2019**, 137, 94.

[46] A. Hadadzadeh, B. S. Amirkhiz, M. Mohammadi, *Mater. Sci. Eng. A* **2019**, 739, 295.

[47] EOS GmbH, Electro Optical System, https://www.eos.info/en/additive-manufacturing/3d-printing-metal/eos-metal-systems/eos-m-290. Accessed March **2020**.

[48] D. Gu, F. Chang, D. Dai, J. Manuf. Sci. Eng. 2015, 137, 021010.

[49] A. Aversa, M. Lorusso, G. Cattano, D. Manfredi, F. Calignano, E. P.Ambrosio, S. Biamino, P. Fino, M. Lombardi, M. Pavese, J. Alloy Compd. 2017, 695, 1470-78.

[50] A.H. Maamoun, M. Elbestawi, G.K. Dosbaeva, S.C. Veldhuis, Addit. Manuf. 2018, 21, 234-47.

[51] ASTM E407, *Standard Practice for Microetching Metals and Alloys*, ASTM International: West Conshohocken, PA, USA **2017**.

[52] ASTM G99, *Standard Test Method for Wear Testing with a Pin-on-Disk Apparatus*. ASTM International: West Conshohocken PA, USA. **2017**.

[53] N. Kang, P. Coddet, H. Liao, T. Baur, C. Coddet, *Appl. Surf. Sci.* **2016**, 378, 142.

[54] I. Rosenthal, A. Stern, N. Frage, *Metallogr.Microstruct. Anal.* **2014**, 3, 448.

[55] G. K. L. Ng, A. E. W. Jarfors, G. Bi, H. Y. Zheng, *Appl. Phys. A* **2009**, 97, 641.

[56] I. Maskery, N. T. Aboulkhair, M. R. Corfield, C. Tuck, A. T. Clare, R. K. Leach, R. D. Wildman, I. A. Ashcroft, R. J. M. Hague, *Mater. Charact.* **2016**, 111, 193.

[57] C. Weingarten, D. Buchbinder, N. Pirch, W. Meiners, K. Wissenbach, R. Poprawe, *J. Mater. Process. Technol.* **2015**, 221, 112.

[58] D. Gu and Y. Shen, *Mater. Des.* **2009**, 30, 2903.

[59] D. Gu and Y. Shen, *J. Alloys Compd.* **2007**, 432, 163.

[60] X. Zhou, X. Liu, D. Zhang, Z. Shen, W. Liu, *J. Mater. Process. Technol.* **2015**, 222, 33.

[61] W. J. Sames, F. A. List, S. Pannala, R. R. Dehoff, S. S. Babu, *Int. Mater. Rev.* **2016**, 61, 315.

[62] M. Giovagnoli, M. Tocci, A. Fortini, M. Merlin, M. Ferroni, A. Migliori, A. Pola, *Mater. Sci. Eng. A* **2021**, 802, 140671.

[63] S. Tammas-Williams, P.J. Withers, I. Todd, P.B. Prangnell, *Scr. Mater.* **2016,** 122, 72**.**

[64] G. Straffelini, A. Molinari, *Wear* **1999**, 236, 328.

[65] N. T. Aboulkhair, C. Tuck, I. Ashcroft, I. Maskery, N. M. Everitt, *Metall. Mater. Trans. A* **2015**, 46A, 3337.

[66] N. Hansen, *Scr. Mater.* **2004**, 51, 801.

[67] L. Girelli, M. Giovagnoli, M. Tocci, A. Pola, A. Fortini, M. Merlin, G.M. La Vecchia, *Mater. Sci. Eng. A* **2019**, 748, 38

[68] E. A. Jaegle, Z. Sheng, L. Wu, L. Lu, J. Risse, A. Weisheit, D. Raabe, *Jom* **2016**, 68, 943.

[69] X. Y. Li, K. N. Tandon, *Wear* **2000**, 245, 148.

[70] P. K. Deshpande, R. Y. Lin, *Mater. Sci. Eng. A* **2006**, 418, 137.

[71] T. K. A. Jaleel, N. Raman, B. Sanjay Kumar, K. S. Sreenivasa Murthy, *Aluminium* **1984**, 60, 787.

[72] Z. H. Xiong, S. L. Liu, S. F. Li, Y. Shi, Y. F. Yang, R. D. K. Misra, *Mater. Sci. Eng. A* **2019**, 740, 148.

[73] Y. J. Liu, Z. Liu, Y. Jiang, G. W. Wang, Y. Yang, L. C. Zhang, *J. Alloys Compd.* **2018**, 735, 1414.

[74] M. Tocci, A. Pola, L. Girelli, F. Lollio, L. Montesano, M. Gelfi, *Metals* **2019**, 9.

[75] P. Wei, Z. Chen, S. Zhang, X. Fang, B. Lu, L. Zhang, Z. Wei, *Mater. Charact.* **2021**, 117, 110769.

[76] W. H. Kan, S. Huang, Z. Man, L. Yang, A. Huang, L. Chang, Y. Nadot, J. M. Cairney, G. Proust, *Wear* **2021**, 482-483, 203961.

[77] W. H. Kan, Y. Nadot, M. Foley, L. Ridosz, G. Proust, J. M. Cairney, *Addit. Manuf.* **2019**, 29, 100805.

[78] P. Thasleem, B. Kuriachen, D. Kumar, A. Ahmed, M. L. Joy, *J. Tribol.* **2021**, 143, 051111-1.

[79] A. K. Mishra, R. K. Upadhyay, A. Kumar, *J. Tribol.* **2021**, 143, 021701-1.

[80] S. Jahanmir, Friction and wear of ceramics, CRC Press, 1993.

[81] V. Abouei, H. Saghafian, S.G. Shabestari, M. Zarghami, Mater. Des. 2010, 31, 3518-3524

The sliding wear behavior of AlSi10Mg alloy manufactured by laser-based powder bed fusion and by gravity casting methods is investigated in the as-produced condition and after T6 heat treatment. As-built AM

samples exhibit the highest wear resistance, while after T6 they show a worsen behavior than the GC samples. Porosity enlargement after T6 and the different Si morphology can explain these findings.